Wind Resistance Evaluation of Existing Standing Buddha Statue Using 3D Laser Scanning and CFD

ABSTRACT

Underestimating the aerodynamic forces acting on structures can lead to them sustaining severe damage. Currently, there are limited studies on the wind flow around complex-shaped tall structures such as the Buddha statue and the aerodynamic forces acting on them. This study discusses the applicability of 3D terrestrial laser scanning in the 3D modeling of an existing complex-shaped standing Buddha statue. This study also aims to shed light on the wind resistance evaluation for the maintenance of a contemporary standing Buddha statue. Large Eddy Simulation (LES) was utilized to calculate the wind flow around it. The results showed that there was no recirculation region at its top. The horseshoe vortex moved closer to the Buddha statue as the angle of attack (AOA) increased. However, the size of the wake region decreased. Sudden changes in the aerodynamic force coefficients and Strouhal number were observed in the Buddha statue—owing to vortices caused by the cross-sectional variations in shape and a setback. Finally, the most vulnerable parts of the Buddha statue which might require optimal maintenance and renovation are mentioned. Results from this study can be used in developing maintenance techniques for similar complex-shaped structures.

Keywords: Complex-shaped tall structure, standing Buddha statue, 3D terrestrial laser scanning, wind resistance evaluation, flow field characteristics, maintenance and renovation

INTRODUCTION

Increasing inbound and outbound tourism usually creates various types of jobs, increases the gross domestic product (GDP), and promotes cross-cultural communication. Thus, many countries strive to possess distinct natural and artificial landmarks. Generally, natural landmarks include geological characteristic features, such as mountains or plateaus, while artificial landmarks include innovative and distinctive buildings. Accordingly, churches with spires; minarets—usually near mosques; and Buddha statues with different mudras, which are often very tall and noticeable even from far distances; have been built to serve as landmarks. According to historical records, structures that are improperly maintained can sustain severe damage and result in serious

human casualties. To avoid this, high-rise structures require regular proper maintenance. However, there are still limitations as most available building codes only provide information on basic shapes such as rectangular and circular cylinders and recommend wind-tunnel testing or numerical simulations for complex-shaped structures instead. If wind tunnel testing is infeasible owing to technical unavailability, financial restrictions, and existing structural conditions, which is especially common in developing countries, computational fluid dynamics (CFD) simulation can be used to fill this gap.

Generally, the structural specifications and external configurations of the structure are required to perform CFD simulations. This type of information can be obtained from architectural drawings, detailed structural drawings, computer-aided design (CAD) files, and structural analysis models. However, such sources may be unavailable for historical monuments or existing structures with unknown or unverified construction details. Therefore, alternative advanced technologies, such as the geographic information system (GIS); light detection and ranging (LIDAR); airborne laser scanning (ALS), drone 3D modeling; and 3D terrestrial laser scanning, are widely utilized. Among them, the 3D terrestrial laser scanning method has become quite popular for obtaining the detailed structural configurations of existing structures. Hess et al. (2018) also used this method to acquire data for the structural health assessment, visualization, and analysis of the Baptistery of St John in Florence, Italy. However, the applicability of 3D terrestrial laser scanning for existing tall and complex-shaped structures is still unclear and further research is required. In the CFD simulation, the accuracy of the simulation is affected by the handling of the complex geometry and grid resolution of the structure by the mesh generation method. Mavriplis (2007, 2008) discussed that the unstructured mesh performed better than the structured meshes in parallel computations. However, using an unstructured mesh may not always be the best approach for addressing complex geometrics and/or adaptive meshing requirements. When the wind load acting on a standard tall building was calculated, the Large Eddy Simulation (LES) results agreed well with the experimental results in the along-wind and across-wind load calculations, while the torsional wind load showed some discrepancies. Therefore, Dagnew and Bitsuamlak (2013) summarized that overall, LES seemed suitable for wind load evaluation. Phuc et al. (2018) also mentioned that the Smagorinsky model agreed well with the wind tunnel experimental results for isolated rectangular high-rise buildings under uniform flow.

Irwin et al. (2008), and Irwin (2010) stated that the structures buffeted by the wind experienced push and pull in the direction perpendicular to the wind flow, and a vortex formed on the side of the structures. When these vortices are alternatively organized in patterns and rock the building from each side, the resulting impact can be severe. This impact can be reduced by modifying the aerodynamic design of tall buildings using various shaping strategies. Baker et al. (2007) stated that even for the highest tower in the world, the Burj Khalifa (Burj Dubai), a "Y" shaped plan was implemented to reduce the aerodynamic forces acting on the tower. Additionally, the setbacks of the Burj Dubai building were designed to change the building width according to the height so that the vortices could not harm the building.

Figure 1 shows the mean flow topology around the basic finite circular cylinder, separated into three areas: the horseshoe vortex, separated flow over the free end, and the wake region. A horseshoe vortex is formed on the ground when the upstream flow separates owing to an adverse pressure gradient. This vortex can cause material elimination at the cylinder-wall junction, which can lead to failure of the pier, bridge, and pylon. An arch vortex is formed in the rear recirculation region, known as the wake region. This vortex and the trailing vortices, which are located downstream of the reattachment, enhance the complexity of the flow structures and create a strong turbulent flow around the finite circular cylinder (Pattenden et al. 2005).

In this study, the 3D terrestrial laser scanning (TLS) method was used to capture the external configuration of a complex-shaped tall Buddha statue, and the scanned data were used to construct the 3D configuration of the statue. Hence, the present study filled an existing gap in the applicability of 3D terrestrial laser scanning on the existing complex-shaped structure. LES, the Smagorinsky model (Smagorinsky, 1963), and unstructured mesh methods were used to investigate the wind flow around the Buddha statue. The paper is organized according to the following sections. First, the paper presents basic information regarding the target Buddha statue, 3D laser scanning, and LES. Then, it describes the characteristics of the 3D flow field around the Buddha statue, and it discusses the aerodynamic force coefficients, vortex shedding frequency, and Stouhal number of the Buddha statue. Finally, the paper mentions the parts of the Buddha statue that require careful treatment during maintenance and renovation. This paper also summarizes the flow characteristics around different parts of the Buddha statue and highlights the most vulnerable parts of it which should be noted for disaster prevention of similar structures in real practice.

LAYKYUN SEKKYA STANDING BUDDHA STATUE

The "Laykyun Sekkya Standing Buddha Statue," also known as the "Maha Bodhi Ta Htaung Standing Buddha," is the sculpture of the Gautama Buddha that is used as a model in this study. It is a hollow-type Buddha statue. It is located on the Po Khaung Mountain, Monywa City, Sagaing Region, Myanmar. The overall height of the statue is approximately 129 m with the lotus throne and 116 m without it. The statue was constructed between 1996 and 2008 with the aim of becoming an attraction site in the Sagaing region. For constructing the statue, reinforced concrete was used from the foundation to the 10^{th} story, steel was used from the 11^{th} story to the neck, and fiberglass was used for the head. As shown in Figure 2, the Laykyun Sekkya Standing Buddha Statue is recorded as the third tallest statue in the world, as of 2022. The case study area, Monywa, has a hot semi-arid climate with extremely hot early monsoon months. Tropical cyclone tracks in the Bay of Bengal have indicated that tropical cyclones originated mostly from the southwest of Monywa, during 1983–2012 (Hirano, 2021). From 2000 to 2010, three tropical cyclones affected this area with maximum sustained wind speeds of 35, 50, and 135 km h^{-1} (UNDP, 2011). Consequently, there is growing concern among residents about the safety of the Buddha statue.

THREE-DIMENSIONAL SCANNING AND MODELING

Recent developments in remote sensing and data acquisition technology have made structural health monitoring and assessment more flexible and time-efficient. However, there are still some limits and boundaries in applying these technologies in existing complex-shaped tall structures. Therefore, this study intends to introduce the 3D modeling procedure of a structure, in which the design information is unavailable, and shape is complicated to manually reproduce. In this study, the 3D terrestrial laser scanning method was used to collect data on the geometry of the Buddha statue as the availability of the CAD data and structural design information is limited to this structure. This method also requires only a few input parameters and can provide accurate measurement within a short period. The collected scan data were mainly pre-processed and inputted into the 3D model using FARO SCENE software (FARO Technologies, Inc., USA).

Terrestrial Laser Scanning (TLS)

A mid-range ground-based terrestrial-type phase-shift laser scanner, Faro Focus 3D X 330, was used to obtain the exterior configuration of the Buddha statue. The scanner collects information such as the size, shape, and texture of the object using a movable infrared laser light line. In addition, it also takes images with an onboard camera to color the point cloud. Hence, it is necessary to prevent moving obstacles such as humans and animals from interfering during 3D laser scanning as this hinders scan recognition and the registration of global coordinates. The polar coordinates of the distance, vertical angle, and horizontal angle are obtained from the mirror and horizontal rotations of the scanner and these coordinates are transformed into Cartesian coordinates. The targeted structure is recorded as a "point cloud," which contains a set of points with each point containing coordinates of the location of the structure in space.

To obtain the optimal view of the Buddha statue with its overall height, minimal obstruction, and sufficient overlap, 36 locations were used, as illustrated in Figure 3 (a). The scanner captured detailed information on the lotus throne and the lower parts of the Buddha statue from 11 blue points, the middle parts of the Buddha statue from 14 violet points, and the head, shoulder, and remaining top parts of the Buddha statue from 11 yellow points. One random draft scan is illustrated in Figure 3 (b). The overlap between each scan location was maintained at 60% because the targetless scanning method was applied. The scans from the two red points were not used in the visualization process because of obstructions. The distance from the Buddha statue to the furthest scanner location was 303.74 m and the maximum probable error for a single point within this distance was 24.3 mm. The equipment settings and scanning duration at one location were within approximately 30 min for ½ resolution and 3× quality color scans. The resolution determines the density of data points and the distance between those points. The "½ resolution" is equivalent to approximately 3.068 mm point spacing at a 10 m distance. Scan quality determines the noise in the measurement based on the incoming signal strength by increasing the observation time. The quality factor 3× has an observation time of approximately 6 µs per scan point. Built-in sensors such as global positioning system (GPS), compass, inclinometer, and altimeter were used together with far distance optimization setting to modify the point cloud during scan registration. The far distance optimization setting considers the distance between the scanner and statue to be larger than 20 m and only focuses on the measurement accuracy of objects located in the far distances.

3D Modelling

The coordinate data were sorted, and point clouds were also extracted from all the 34 panorama 360° draft scans of the Buddha statue. First, the initial alignment was performed by manually identifying the mutual parts of each scan. Then, the Buddha statue was simply divided into four clusters with customized automatic scan-to-scan alignment. After all the clusters were roughly aligned, the common reference planes and points were used to position these clusters into one global coordinate system, as illustrated in Figure 4. The total alignment error for the 3D modeling of the Buddha statue was 23.4 mm. The average point spacing of the 3D statue model was approximately 0.1 m.

During the generation of the project point cloud dataset, there were limitations in extracting data from the draft scans for black surfaces of the Buddha Statue, such as the hair and glasses parts. Generally, a black surface has a slight or no reflectivity. The poor reflectivity of the black surface and the sky-high height of the Buddha statue made it difficult for the 3D laser scanner to capture data from these areas. Therefore, the hair part of the Buddha statue was manually reproduced using FreeCAD software due to its low point density. The height (H), width (B), and side length (L) of the Buddha statue at the base were 129, 47.63, and 43.47 m, respectively. Since the exterior configuration of the statue was complex, the surface mesh of the 3D model generated from the scans contained twists and overlaps. These meshes were cleaned and repaired into approximately 22 mm meshes using Autodesk Meshmixer. The final 3D replica model of the Laykyun Sekkya Standing Buddha statue is shown in Figure 5. In this study, the total alignment error of the Buddha statue (23.4 mm) was only about 0.02–0.05 % compared to the statue's overall dimension, which was unlikely to change the simulation results in a significant way.

COMPUTATIONAL FLUID DYNAMICS SIMULATION

The unsteady flow field around the standing Buddha statue and its aerodynamic characteristics resulting from its complex shape were calculated by performing LES using OpenFOAM 4.0. The governing equations used were the filtered incompressible Navier–Stokes equations and the equation of continuity:

$$\frac{\partial \overline{u}_i}{\partial x_i} = 0 \quad (1)$$

$$\frac{\partial \bar{u}_i}{\partial t} + \bar{u}_j \frac{\partial \bar{u}_i}{\partial x_j} = -\frac{1}{\rho}\frac{\partial \bar{p}}{\partial x_i} + \frac{\partial}{\partial x_j}\left\{(v + v_{SGS})\left(\frac{\partial \bar{u}_i}{\partial x_j} + \frac{\partial \bar{u}_j}{\partial x_i}\right)\right\} \quad (2)$$

where $\bar{u}_i$ is the filtered velocity, v is the viscosity, $\bar{p}$ is the filtered pressure, ρ is the density, and v_{SGS} is the subgrid-scale eddy viscosity coefficient, which was modeled based on the Smagorinsky model which is represented as follows:

$$v_{SGS} = (C_s f_s \Delta)^2 |\bar{D}| \quad (3)$$

where $\bar{D}$ is the strain rate tensor, Δ is the filter width, f_s is the damping function that corrects the value of v_{SGS} near the wall, and C_s is the Smagorinsky constant, which was set as 0.12.

Computational Domain

Considering that tropical cyclones come mostly from the southwest and that the Buddha statue was designed considering ones that came from the west, four different wind directions were considered during the simulation. These wind directions were noted as the along-wind direction (α = 0°), west (α = 5°), southwest (α = 50°), and across-wind (α = 90°). LES was performed for a finite circular cylinder with the diameter of an average statue's width (B_{avg} = 30.22 m) and height (H = 129 m) to validate the numerical simulations of the Buddha statue. For all the simulation cases, the x-axis was the along-wind direction, and the y-axis was the across-wind direction. The dimensions of the computational domains were determined according to standards specified by the Architectural Institute of Japan (AIJ, 2017). The total computational domain size was 24.5 B (x) × 21 B (y) × 2 H (z), as illustrated in Figure 6 (a). The blockage ratio in the across-wind direction was between 1.57 and 2.5%. Ten probes were embedded inside the computational domain for the interpretation of the flow around the models as shown in Figure 6 (b) and the velocities in the wake region were also recorded. In this study, both the Buddha statue and circular cylinder models were rigid. Both were equally divided into approximately 26 parts (0.039 D each) for a detailed representation of the aerodynamic characteristics of the complex configuration. The topographic effects are neglected in this calculation to study the flow patterns and aerodynamic characteristics produced solely by the Buddha statue.

Surface Mesh and Volume Mesh

Since unstructured-mesh methods were proven to be more convenient and successful in handling complex geometries, one such method, anisotropic tetrahedral mesh generation, was applied to reproduce the complex shape of the Buddha statue using Pointwise (VINAS, Japan), a mesh generation software. As the windows around the Buddha statue did not contribute to the flow separation, they were considered not to affect the simulation and simplified them as a plain surface to reduce the mesh number. Triangle and quad mesh cells were used to generate the surface meshes of the statue. The average spacing between each grid (Δs) was around 0.25 m, which was B/190 (B is the width of the Buddha statue). The meshing is well reflected in the low point density near the top of the statue. The volume mesh was mainly composed of tetrahedral, pyramidal, prism, and hexahedral cells. This allowed us to efficiently reproduce the complex shapes of the Buddha statue and reduce the total grid number. The height of the first cell near the Buddha statue was 0.09 m (B/530) and that of the last cell was 10 m (B/5). The total grid number of each simulation case was approximately between 8.8×10^6 and 10.2×10^6 for different angle of attack (AOA) cases. The meshes near the Buddha staute and the circular cylinder is shown in Figure 6 (c) and (d), respectively.

Boundary Conditions

The logarithmic inlet wind profile was calculated according to Equations (4) and (5), where U is the wind velocity, U^* is the friction velocity, κ is the von Kármán's constant, with a value of 0.41, z is the vertical coordinate, z_0 is the surface roughness height of 0.01 m for exposure category C, z_g is the minimum z-coordinate (in m), and U_{ref} is the reference wind velocity of 31.3 m s^{-1} at 10 m above the ground surface, as specified by the Myanmar National Building Code (MNBC).

$$U = \frac{U^*}{\kappa} ln\left(\frac{z - z_g + z_0}{z_0}\right) \quad (4)$$

$$U^* = \kappa \frac{U_{ref}}{ln\left(\frac{z_{ref} + z_0}{z_0}\right)} \quad (5)$$

At the outlet boundary, the gradient of the velocity in the streamwise direction and pressure was zero. For the ground surface, an atmospheric boundary layer with a roughness length of 0.01 m for open terrains,

belonging to Exposure C, was used as it provided a better turbulence kinematic viscosity for atmospheric velocity profiles. On the model surface, the wall function described in Equation (6), proposed by Spalding (1960), was utilized. For the other surfaces, a slip boundary condition was applied.

$$y^+ = u^+ + \frac{1}{E}\left[e^{\kappa u^+} - 1 - \kappa u^+ - \frac{1}{2}(\kappa u^+)^2 - \frac{1}{6}(\kappa u^+)^3\right] \quad (6)$$

Numerical Algorithms

The first-order implicit Euler method was used for time advancement, and the second-order least squares discretization scheme was followed to compute the gradient terms. All the divergence schemes were calculated based on a second-order linear upwind scheme. For pressure-velocity coupling, the pressure-implicit with splitting of operators (PISO) algorithm was used (Irwin, 2010).

The Reynolds number is defined as $Re = U_H B/\nu$, where U_H is the wind velocity at the height of the model (m/s), B is the width of the model in the along-wind direction (m), and ν is the kinematic viscosity (m^2 s^{-1}). The mean wind velocity at the height of the Buddha statue (U_H) was around 42.88 m s^{-1}, resulting in the statue and circular cylinder having Reynolds numbers of 1.30×10^4 and 2.04×10^4, respectively. The non-dimensional average time is defined as $t^*=U_H t/B$, where t is the physical simulation time. In this study, the simulations were carried out for about 200 t^* to ensure statistical convergence and full flow field development. For further calculation and sampling of the aerostatic force coefficients, an average duration of about 150 t^* after a preliminary calculation of about 50 t^* was used. The time step (Δt) was 5.0×10^{-4} and the maximum Courant number was around 1.5. This guaranteed a stable simulation for an implicit scheme on the unstructured grid. The sampling time was 10 ms (100 Hz), and the sampling number was 20,000.

In this section, the visualization of the flow field around the models is presented in terms of time-averaged normalized velocity magnitude and streamlines (Smits and Lim, 2000). The length of the recirculation region (L_r) is defined as the distance between the centre of the model and the near-wake saddle point in the time-averaged flow field Yoon et al. (2010). The width of the wake region (d') is defined as the lateral distance at a given streamwise location between two points situated on opposite sides of the model centerline, distinguishing

the outer flow from the rotational wake flow (Roshko, 1954). The distance between the centres of the vortices in each pair was measured as the distance between each vortex pair (d_{pair}).

Mean Velocity Profiles

The mean along-wind velocity profiles of probe 3 showed a clear wind velocity acceleration at the top of the circular cylinder model, while the wind velocity was gradually accelerated in all the Buddha statue cases at this point as shown in Figure 7. A similar wind velocity acceleration was observed at the top of both the models in the mean along-wind velocity profile of probe 4. Therefore, the flow separation only occurred closer to the top rear head of the Buddha statue within the studied wind direction regions. In the mean across-wind velocity profiles, considerable variations were observed in-between 0.15 to 0.25 H and 0.7 to 1.0 H at probe 4 for the Buddha statue α = 90° case. Since these changes were the largest among all the simulation cases, the wake flow in these regions were mostly highly asymmetric or unsteady compared to those in the other regions.

Flow Field Around the Circular Cylinder

A horseshoe vortex was observed in front of the circular cylinder model as shown in Figure 8 (a) and (b). At the top part of this model, the flow separated at the leading edge and reattached at the trailing edge. The downwash from the top of the circular cylinder produced massive and small vortices in the upper and lower halves of the wake region, respectively. These flows agreed well with the results in existing literature (Pattenden et al., 2005). As shown in Figure 9 (a), the lower vertical vortex in the *xz*-plane extended from the ground to 0.2 H while the upper vertical vortex extends from 0.25 to 1.0 H. A small horseshoe vortex was observed at 0.88 B from the front surface of the circular cylinder at z/H= 0.006 as shown in Figure 9 (b), indicating 3D boundary layer separation. In the wake region of the *xy*-plane, the two symmetric vortices, which were denoted as a paired vortex, started to appear from 0.06 to 0.37 H with an increasing d' of 0.75 to 0.80 B and L_r of 1.68 to 1.75 B as shown in Figure 9 (c) and (d). However, the values started to decrease after 0.37 H till the top was reached. Since a reduction in the wake width suggested a reduction in the time-averaged momentum loss in the wake region, smaller loadings on the model could be expected in these regions. Near the ground surface, the d_{pair} was 0.25 B. This value increased with increasing height, reaching a maximum of 0.55 B at 0.37 H. Then, this value decreased

with increasing height, reaching a minimum of 0.33 *B* at 0.83 *H*. Therefore, these two vortices were connected as an arch vortex at the top of the wake region as described by previous studies (Pattenden et al. 2005), with the base of the arch vortex quite close to each vortex, contrary to their positions. No obvious vortex was observed behind the circular cylinder on the *xy*-plane after 0.83 *H* while two tip vortices were observed at 1.01 *H*, as in Figure 9 (e) and (f).

Flow Field Around the Buddha Statue

A horseshoe vortex was observed in front of the Buddha statue in all cases, indicating 3D boundary layer separation as shown in Figure 8 (c), (d), (e) and (f). Unlike the circular cylinder, the horseshoe vortex was located further from the front surface of the model, and the smooth and round-shaped head of the Buddha statue, which functioned as a roof, smoothly passed the flow into the wake region. Therefore, flow separation occurred closer to the trailing edge of the Buddha statue. When the wind blew from 0, 5, and 50° AOAs, the model was bluff, resulting in a larger wake, and the slope of the downwash from the top was more moderate than that of the circular cylinder. At α = 90°, the downwash slope was steep, and the vortices in the wake region are different from that in the rest AOAs.

In α = 0° case, as shown in Figure 10 (a), the lower vertical vortex in the *xz*-plane has centre around 0.02 *H* while the upper vertical vortex has centre around 0.72 *H*. A small horseshoe vortex was observed at 1.29 *B* from the front surface at 0.006 *H* as shown in Figure 10 (b). In the wake region of the *xy*-plane, the L_r value decreased from 2.40 to 0.17 *B* with the increase in the statue's height from 0.06 to 0.98 *H*, as shown in Figure 10 (c) and (f). On the other hand, the vortex pair started to appear from 0.06 to 0.37 *H* with an increasing d' value of 0.95 to 1.36 *B* and an increasing d_{pair} value of 0.62 to 1.09 *B* as in Figure 10 (d). However, the d_{pair} value decreased after 0.37 *H*, and the upper vortex from the vortex pair dissolved at 0.71 *H* as shown is Figure 10 (e). Two small vortices were still observed near the statue at 0.75 *H* and no obvious vortex on the *xy*-plane was found afterwards. A small recirculation region was observed at 0.98 *H* where sudden changes in shape between the forehead and top of the statue occurred.

In α = 5° case, as shown in Figure 11 (a), the lower vertical vortex in the *xz*-plane has centre around 0.02 *H* while the upper vertical vortex has centre around 0.70 *H*. A horseshoe vortex was observed at 1.09 *B* from the front surface at 0.006 *H* as shown in Figure 11 (b). However, only one vortex was observed on the

lower side of the *xy*-plane at 0.06 *H* as illustrated in Figure 11 (c). Then, an uneven pair vortex was generated at 0.10 *H* as shown in Figure 11 (d) and developed into similar vortices of $\alpha = 0°$ with a similar mechanism till 0.64 *H*. The two vortices from the uneven vortex pair combined somewhere between 0.67 and 0.71 *H*. Subsequently, no obvious vortices were observed afterward.

In $\alpha = 50°$ case, as shown in Figure 12 (a), the lower vertical vortex in the *xz*-plane has centre around 0.25 *H* while the upper vertical vortex has centre around 0.65 *H*. At 0.006 *H*, the horseshoe vortex was observed at 1.05 *B* from the front surface of the statue as shown in Figure 12 (b). Throughout the statue's overall height, the L_r value varied between 1.81 and 0.20 *B*, and the d' value varied between 0.31 and 0.92 *B*. The vortex generation in the $\alpha = 50°$ case started from the upper side of the *xy*-plane at 0.06 *H*, and then, a vortex pair was developed at 0.14 *H* as shown in Figure 12 (c) and (d). The vortex pair dissolved at 0.56 *H* as in Figure 12 (e) and moved towards the statue as smaller vortices between 0.60 and 0.67 *H*. No obvious vortex was observed around the statue between 0.71 and 0.83 *H* while small vortices could be observed around the statue afterwards as illustrated in Figure 12 (f).

Since the statue was streamlined in the $\alpha = 90°$ case, it had the smallest wake region in this case, and it also had more vortices. As shown in Figure 13 (a), the lower vertical vortex in the *xz*-plane has centre around 0.07 *H*, the middle vertical vortex has centre around 0.52 *H* and the upper vertical vortex has centre around 0.95 *H*. As illustrated in Figure 13 (b), the horseshoe vortex was observed at 0.95 *B* from the front surface of the statue at 0.006 *H*. On the *xy*-plane, the pair vortex was generated starting from 0.10 till 0.33 *H*, with the increasing L_r value of 1.24 to 1.31 *B*, the decreasing d' value of 0.70 to 0.56 *B*, and the d_{pair} value of 0.39 to 0.37 *B* as illustrated in Figure 13 (c) and (d). Afterward, the vortex on the lower side of the wake region (the same side as the setback of the model) became smaller. Only one upper vortex was observed at 0.52 *H* with a L_r of 1.03 *B* and d' of 0.50 *B* as shown in Figure 13 (e). While L_r and d' continued to decrease, no obvious vortex was found within 0.56–0.67 *H*. A small vortex reappeared on the upper side of the wake region at 0.71 *H* and developed into two vortices at 0.75 *H* as illustrated in Figure 13 (f). Later, this was reduced to one vortex on the lower side between 0.79 and 0.83 *H*. This vortex developed into a vortex pair once more between 0.86–0.90 *H*. No obvious vortex was found at 0.94 *H* but a small vortex pair was found again in the wake region at 0.98 *H*.

Hence, we inferred that the width of the wake region was highly influenced by the shape of the model, and that the formation of vortices in the wake region was complex.

WIND RESISTANCE EVALUATION OF BUDDHA STATUE

Wind loading on structures is an important consideration made in structural design, as it can significantly affect the safety of the structure. Furthermore, the effects of wind on structures can be divided into two types: static and dynamic. In this study, the mean aerodynamic force coefficients (C_{Fx}, C_{Fy}) and Strouhal number (St) for the studied cases with different AOAs were calculated to determine how the flow patterns around the Buddha statue could affect its structure.

Aerodynamic Coefficients (C_{Fx}, C_{Fy})

During the LES simulation, the pressure and wind velocity acting on and around the Buddha statue were recorded. The mean wind forces were calculated by integrating the pressure around the surface area of each part. The mean force coefficients were calculated as follows:

$$C_{Fi} = \frac{F_i}{\frac{1}{2}\rho U_{H_j}^2 A_j} \quad (7)$$

where F_i (i = x, y) is the mean force of each model part along the x and y directions, A_j is the frontal surface area of part j, ρ is the air density, and U_{H_j} is the mean wind speed at the mid-height of part j.

The mean wind force coefficients of the circular cylinder and Buddha statue are shown in Figure 14. The mean along-wind force coefficient (C_{Fx}) of the circular cylinder model was 1.53 at 0.02 H and within 0.86–1.06 between 0.06–0.94 H. The C_{Fx} value changed from following a decreasing trend to following an increasing one around 0.33 H where the main upper and lower vertical vortices were reattached vertically on the xz-plane. At 0.98 H, the value of C_{Fx} decreased to 0.69, which might be related to the disappearance of the horizontal vortex pair on the xy-plane. For the across-wind force coefficient (C_{Fy}), the value throughout the height was approximately zero. Therefore, the flow separation was symmetrical, and the pressure distributions on both sides of the circular cylinder were equal in the across-wind direction.

Sharp changes in both the C_{Fx} and C_{Fy} values were found around 0.14–0.25 H and 0.83–0.90 H of the Buddha statue in the studied wind directions. In the first region, the shape of the Buddha statue changed from rectangular to elliptical. In this region, the lower vertical vortex was reattached vertically on the xz-plane, accompanied by a horizontal vortex pair and a large wake region. Therefore, the value of C_{Fx} suddenly increased in this area. The second region was located around the neck of the Buddha statue. Here, the upper vertical vortex was reattached vertically on the xz-plane, whereas the horizontal vortex pair weakened on the xy-plane. The C_{Fx} value decreased steadily with the height from 1.69 to 0.70 for α = 0°, 1.70 to 0.70 for α = 5°, and 1.27 to 0.74 for α = 50° between 0.25 and 0.83 H. This decrease was attributed to the reduction in the wake region and vortex size near the top of the Buddha statue. However, the value of C_{Fx} remained constant between 0.29 and 0.52 H in the α = 90° case. Since the elevator setback behind the statue ended at 0.56 H, the horizontal vortex pair transformed into a single vortex and the C_{Fx} value started to decrease from the stabilized condition until it reached 0.87 H. The C_{Fx} value of the α = 90° case was the smallest among the C_{Fx} values in all the cases because the wake region was the smallest. Similar sudden changes were observed in the C_{Fy} values. Symmetric time-averaged flow was observed only between 0.19 to 0.77 H in the α = 0° case.

When the wind direction for the Buddha statue changed from 0° to 90°, the flow separation from the top remained the same. However, the slope of the downwash became steeper as illustrated in Fig. 8. This decreased the length of the recirculation region (L_r). The width of the Buddha statue decreased from 47.63 to 43.47 m as AOA increased. Therefore, the width of the wake region (d') and distance between each vortex pair (d_{pair}) also decreased. As a result, the size of the overall 3D wake region behind the Buddha statue became narrower and the global mean along-wind force coefficient value decreased constantly from 1.35, 1.35, 1.08, and 0.80. On the other hand, the global mean across-wind force coefficient varied from 0.01, 0.14, -0.40, and 0.40. Therefore, it was concluded that symmetric time-averaged flow was still observed at α = 0° despite the complex shape of the Buddha statue.

Strouhal Number (*St*)

Previous studies have shown that a large amount of wind load is placed on tall structures owing to vortex shedding in the wake region behind them. According to Irwin (2010), the effects of vortex shedding on a tall building can be determined by comparing the fundamental frequency of vibration for the building (f_b) and vortex

shedding frequency from the building into the vortex street (f_v), where f_b is mainly dependent on the structural system and mass distribution of the building. The Strouhal number (*St*) can be calculated as follows:

$$St = \frac{f_v U_{H_j}}{w_j} \tag{8}$$

where U_{H_j} is the mean wind velocity at the mid-height of part *j*, w_j is the width of part *j* in the along-wind direction, and f_v is the vortex shedding frequency.

Figure 15 (a) shows the vortex shedding frequency (f_v) in all the measured cases. The f_v value of the Buddha statue was approximately constant throughout the height for α = 0 and 5°, and the value was approximately half that of the circular cylinder. However, an increase in the f_v value was observed within 0.40–0.70 *H* in the α = 50° case, while the remaining heights had similar values of α = 0 and 5°. The α = 90° case, wherein the setback was attached parallel to the inlet wind direction, had the highest f_v value. As this case had the minimum d' and L_r values, the spacing between the vortices was small, and the f_v value increased. Additionally, a phenomenon that occurred in the α = 50° case also similarly occurred in this case, starting from 0.70 *H*. This may be related to the creation of asymmetric vortices due to the flow changes in the wake region. Furthermore, the power of these frequencies was weak and difficult to capture.

The Strouhal number of the circular cylinder used in this study agreed well with the results reported by Fox and West (1993). According to the static wind tunnel tests performed by Ma et al. (2017), the Strouhal number of an elliptical cylinder is 0.18 for $Re = 1.24 \times 10^5$ and α = 26°. As the Strouhal number depends on the width, wind speed, and vortex shedding frequency, variations in the *St* value were observed between each height in all the cases, as shown in Figure 15 (b). The *St* value in all the cases decreased steadily from their starting values during the interval between the ground and 0.16 *H* due to the influence of the 3D boundary layer separation. Meanwhile, the *St* values in all the cases except the α = 50° case were approximately close to each other between 0.16 and 0.74 *H*. In the α = 50° case, the *St* value became closer to the others only within 0.16–0.47 *H* due to the exposure of setback to the inlet wind flow. Afterwards, the value increased to approximately twice that in the remaining cases until the height reached 0.70 *H*. Later, the value decreased, similarly following the trend that the values in the other cases did for the remaining height. A similar abrupt change in the *St* value

was also observed starting from 0.70 H in the α = 90° case. The St value of the Buddha statue increased from 0.094 to 0.118 as the AOA increased between 0.16 and 0.47 H in all cases. Therefore, the statue might vibrate at lower wind velocity when the AOA increased in this region. Furthermore, the abrupt change in the St value increased with height, especially toward the top of the Buddha statue as the AOA increased. Thus, wind-induced vibration responses of this structure may vary largely depending on the height and AOA.

MAINTENANCE, RENOVATION, AND MANAGEMENT

The 3D terrestrial laser scanning is a simple process and the conditions around the Buddha statue can be inspected easily from the scanned data visualizations. These data can be combined with mapping or geological data obtained from the GIS and used in building information modelling (BIM) for the maintenance, rehabilitation, and management of the Buddha statue. In this study, wind load characteristics such as aerodynamic force coefficients and vortex shedding frequencies were calculated based on a 3D model obtained by scanning to complex-shaped. Afterward, the most vulnerable parts of the Buddha statue which might require maintenance were noted based on the numerical investigation results acquired using 3D visualization data.

Based on the flow field analysis around the Buddha statue, it was expected to obtain higher along-wind forces at α = 0 and 5°. For all studied AOAs, the along-wind force coefficient was largest at the base and decreased toward the top as shown in Figure 14. Therefore, the lower part of the statue, such as under 0.2 H, may require strengthening as time passed. Furthermore, both the C_{Fx} and C_{Fy} values indicated that sudden force changes could occur within 0.14–0.25 H and 0.83–0.90 H. This may have a noticeable influence on the serviceability and structural safety of the Buddha statue on closer inspections. Hence, the strength of the connection between the lotus throne and the feet (0.14–0.25 H) and neck (0.83–0.90 H) of the Buddha statue need to be increased during its maintenance and renovation. As the statue has relatively a small mass as it is a hollow structure, whether wind loading governed the lateral load design of the statue should be checked during the analysis for the maintenance and renovation. Additional vertical and diagonal bracings could be added inside the statue to increase wind load resistance if it is necessary. The strength of these bracings should be checked and strengthened on a timely basis, to efficiently reduce the effects of wind-induced loads on the statue.

As the height of the statue becomes higher, the natural frequency is expected to become smaller as the statue becomes slender and the setback behind the statue discontinues. On the other hand, the Kármán vortex shedding frequency became higher as the AOA increased. Resonant (lock-in) wind load will arise when the vortex shedding frequency is close to the natural frequency of the structure. In addition, this can induce vibrations that decrease occupant comfort, reduce serviceability and lead to structural failure. If the accelerometer, impact test, and modal analysis are possibly to be carried out, the natural frequency of the Buddha statue could be calculated. Then, the resonant wind load on the Buddha statue can be determined based on the Kármán vortex shedding frequency values provided in this study, and the proper maintenance and renovation plan for the Buddha statue can be implemented for each story level. Therefore, appropriate preventative measures for noticeable vibrations may be possible in the future design of a similar structure.

Since the across-wind response dominates wind loading at higher wind speeds and is mainly caused by vortex shedding, many structures modify the shapes around their corners, cross-sections, and heights to reduce the amount of wind loading and vibrations caused by vortex shedding. In the Buddha statue under study, one setback was present at the back between 0.14 and 0.56 H. After this setback, abrupt changes in the Strouhal number were observed. The locations where these abrupt changes occurred moved to a higher height with the increase in the AOA. Since the increase in Strouhal number means an increase in instability, aerodynamic modification such as slotted corners, baffles, and fins should be considered when renovating to reduce the instability of the Buddha statue.

The horseshoe vortex, which was observed upstream, moved closer to the Buddha statue with an increased AOA, as listed in Table 1. Hence, the construction materials between the ground surface and 0.10 H should be strengthened periodically to withstand material deterioration and avoid collapse during high winds such as tropical cyclones. The Buddha statue has a large wake with L_r of 2.64B and d′ of 1.36B. This may significantly affect the wind flow field and wind load acting on the surrounding structures. This should also need to consider in the structural management of the surrounding structures.

CONCLUSIONS

In this study, the wind resistance of an existing complex-shaped standing Buddha statue was evaluated using 3D terrestrial laser scanning and Large Eddy Simulation (LES). Flow visualization was performed to obtain a full picture of the flow around the statue and to investigate the flow structures in the separation regions for different shapes of the statue. Based on the results, the following conclusions were drawn regarding 3D laser scanning; and the flow field characteristics, aerodynamic characteristics, and management of the Buddha statue.

(1) As black surfaces have less reflectivity and cannot return sufficient laser pulses to create a point cloud, the scanner could not collect complete data on the black hair of the Buddha statue. These imperfections can be treated with third-party software. The 3D terrestrial laser scanning method was easy to operate and could reproduce fairly precise 3D models of massive, tall, and complex-shaped structures within a short period of time.

(2) Owing to the variations in the surface, cross-sectional shape, and the presence of setbacks throughout the height of the Buddha statue, the flow field around the statue contained many small vortices, and the 3D arch vortex in the wake region intertwined in a complex manner. The time-averaged flow fields in the *xz*-plane and different *xy*-planes of the studied cases with different angle of attacks (AOA) showed that the wake region size decreased and the horseshoe vortex moved closer toward the Buddha statue as the AOA increased. Furthermore, the size of the wake region depended not only on the width of the model, but also on the flow separation conditions. Tip vortices were not observed at the top of the Buddha statue, whereas a small recirculation zone was observed on the windward side at the top. Therefore, the vortex shedding near the top was different from that at the remaining height, and the interaction between the flow and leading edge was very small at the top of the Buddha statue. The Strouhal number of the Buddha statue increased and the abrupt changes in the value moved towards the top of the Buddha statue as the AOA increased. Hence, this structure is likely to be affected by flow-induced vibrations when the AOA changed and this also needs to be considered in the structural design and maintenance.

(3) The Buddha statue behaved as a bluff body when the AOAs were 0, 5, and 50°, whereas it behaved as a streamlined body at 90°. Accordingly, the α = 90° case had the smallest wake region size and minimum along-wind force coefficient among the studied cases. Based on the across-wind force coefficient, the symmetric time-averaged flow was only observed within 0.19–0.77 *H* under the α = 0° case. The presence of a setback on the back of the Buddha statue increased the Strouhal number after 0.50 *H* for cases with higher AOAs. This

abrupt increase moved towards a higher height as the AOA increased. Furthermore, the horseshoe vortex with 0.10 *H* moved closer toward the Buddha statue as the AOA increased. Therefore, these places should be regularly inspected for maintaining the safety of the Buddha statue and protecting it against natural and man-made disasters.

Laser scanning the Buddha statue, which was surrounded by mountainous terrains and a dam; and meshing and simulating the complex-shaped Buddha statue with the setback on its back were some of the challenges encountered during this study. To address these large challenges, various unconventional methods were required. With the higher demand for economical and time-efficient methods for accurate wind response evaluation, the methods highlighted in the previous sections can be considered in evaluating tall complex-shaped structures where field testing is difficult or infeasible. In the future, more research on long-term structural health monitoring, life-cycle performance evaluation, and the risk analysis of unique structures should be conducted. It is also an alternative to apply power law and consider topographic effects in the future simulation.

DATA AVAILABILITY STATEMENT

All data, models, or codes that support the findings of this study are available from the corresponding author upon reasonable request.

ACKNOWLEDGEMENTS

We would like to express our heartfelt gratitude to the late Professor, Dr. Hiromichi Shirato, Department of Civil and Earth Resources Engineering, Kyoto University, for the indispensable guidance and advice. We also express our deep gratitude to the late president of the Myanmar Engineering Society (Monywa), Engr. Aung Kyaw Myint, for help during 3D laser-scanning. We are grateful to the Assistant Director, Dr. Kyaw Zaya Htun, Remote Sensing, and GIS Research Center, Yangon Technological University (YTU); Engr. Thant Zin Win; and the students from YTU for their interest and help during the laser-scanning trip. The supercomputer of ACCMS, Kyoto University, was used for flow simulation.

DECLARATION OF INTEREST STATEMENT

The authors report there are no competing interests to declare.

REFERENCES

AIJ (Architectural Institute of Japan). 2017. Guidebook of Recommendations for Loads on Buildings 2. Wind-induced Response and Load Estimation/Practical Guide of CFD for Wind Resistant Design, Architectural Institute of Japan, (in Japanese).

Baker, W. F., D. S. Korista, and L. C. Novak. 2007. "Burj Dubai: Engineering the world's tallest building." *Structural Design of Tall and Special Buildings*, 16 (4). https://doi.org/10.1002/tal.418.

Dagnew, A. K., and G. T. Bitsuamlak. 2013. "Computational evaluation of wind loads on buildings: A review." *Wind and Structures, An International Journal*.

Fox, T. A., and G. S. West. 1993. "Fluid-Induced loading of cantilevered circular cylinders in a low-turbulence uniform flow. Part 1: Mean loading with aspect ratios in the range 4 to 30." *Journal of Fluids and Structures*, 7 (1). https://doi.org/10.1006/jfls.1993.1001.

Hess, M., V. Petrovic, M. Yeager, and F. Kuester. 2018. "Terrestrial laser scanning for the comprehensive structural health assessment of the Baptistery di San Giovanni in Florence, Italy: an integrative methodology for repeatable data acquisition, visualization and analysis." *Structure and Infrastructure Engineering*, 14 (2). https://doi.org/10.1080/15732479.2017.1349810.

Hirano, A. 2021. "Effects of climate change on spatiotemporal patterns of tropical cyclone tracks and their implications for coastal agriculture in Myanmar." *Paddy and Water Environment*, 19 (2). https://doi.org/10.1007/s10333-021-00842-x.

Irwin, P. A. 2010. "Vortices and tall buildings: A recipe for resonance." *Physics Today*, 63 (9). https://doi.org/10.1063/1.3490510.

Irwin, P., J. Kilpatrick, J. Robinson, and A. Frisque. 2008. "Wind and tall buildings: Negatives and positives." *Structural Design of Tall and Special Buildings*.

Ma, W., J. H. G. Macdonald, and Q. Liu. 2017. "Aerodynamic characteristics and excitation mechanisms of the galloping of an elliptical cylinder in the critical Reynolds number range." *Journal of Wind Engineering and Industrial Aerodynamics*, 171. https://doi.org/10.1016/j.jweia.2017.10.006.

Mavriplis, D. J. 2007. "Unstructured mesh discretizations and solvers for computational aerodynamics." *Collection of Technical Papers - 18th AIAA Computational Fluid Dynamics Conference*.

Mavriplis, D. J. 2008. “Unstructured-mesh discretizations and solvers for computational aerodynamics.” *AIAA Journal*.

MNBC (Myanmar National Building Code). 2016. Part 3: Structural Design, Myanmar National Building Code, Second Edition.

OpenFOAM. 2019. OpenFOAM v6 User Guide: 4.4 Numerical Schemes, Retrieved from https://cfd.direct/openfoam/user-guide/v6-fvschemes/.

Pattenden, R. J., S. R. Turnock, and X. Zhang. 2005. “Measurements of the flow over a low-aspect-ratio cylinder mounted on a ground plane.” *Experiments in Fluids*, 39 (1). https://doi.org/10.1007/s00348-005-0949-9.

van Phuc, P., T. Nozu, H. Kikuchi, K. Hibi, and Y. Tamura. 2018. “Wind pressure distributions on buildings using the Coherent structure smagorinsky model for LES.” *Computation*, 6 (2). https://doi.org/10.3390/COMPUTATION6020032.

Roshko. 1954. “On the drag and shedding frequency of two-dimensional bluff bodies.” *NACA Technical Note 3169*, (July 1954).

Smagorinsky, J. 1963. “General circulation experiments wiht the primitive equations I. The basic experiment.” *Monthly Weather Review*, 91 (3).

Smits, A. J., and Lim, T. T. (2000). Flow Visualization: Techniques and Examples, Imperial College Press, First edition.

Spalding, D. B. 1960. “A single formula for the ‘law of the wall.’” *Journal of Applied Mechanics, Transactions ASME*, 28 (3). https://doi.org/10.1115/1.3641728.

UNDP (United Nations Development Programme). 2011. Multi Hazard Risk Assessment in Rakhine State of Myanmar, Final Report, December.

Yoon, D. H., K. S. Yang, and C. B. Choi. 2010. “Flow past a square cylinder with an angle of incidence.” Physics of Fluids, 22 (4). https://doi.org/10.1063/1.3388857.

TABLES

Table 1. Location of horseshoe vortex

Angle of attack, α (°)	Distance from the front surface of the Buddha statue (B)
0	1.29
5	1.09
50	1.05
90	0.95

LIST OF FIGURE CAPTIONS

Fig. 1. Sketch of the time-averaged flow around the finite circular cylinder (Not in scale).

Fig. 2. Laykyun Sekkya Standing Buddha Statue.

Fig. 3. (a) Scanner locations (Maps Data: Google, ©2018 CNES/ Airbus, DigitalGlobe) (b) Draft scan at the base viewpoint.

Fig. 4. (a) Unregistered scan (b) Targets at two different scans (c) Project point clouds.

Fig. 5. 3D model of the Buddha statue.

Fig. 6. (a) Computational domain dimension (Not in scale) (b) Locations of the probe (c) Mesh around the Buddha statue and (d) Mesh around the circular cylinder

Fig. 7. Mean velocity profiles in the wake region at probes 3, 4, 9, and 10.

Fig. 8. 3D mean velocity streamlines around circular cylinder: (a) side view (b) top view; and around Buddha statue: (c) side view at $\alpha = 5°$ (d) side view at $\alpha = 50°$ (e) side view and (f) top view at $\alpha = 90°$.

Fig. 9. Time-averaged flow field around the circular cylinder on (a) xz-plane at y/B=0 and xy-plane at (b) 0.006, (c) 0.06, (d) 0.37, (e) 0.83, and (f) 1.01 H.

Fig. 10. Time-averaged flow field around the Buddha statue at $\alpha = 0°$ on (a) xz-plane at y/B=0 and xy-plane at (b) 0.006, (c) 0.06, (d) 0.37, (e) 0.71, and (f) 0.98 H.

Fig. 11. Time-averaged flow field around the Buddha statue at $\alpha = 5°$ on (a) xz-plane at y/B=0 and xy-plane at (b) 0.006, (c) 0.06, and (d) 0.10 H.

Fig. 12. Time-averaged flow field around the Buddha statue at $\alpha = 50°$ on (a) xz-plane at y/B=0 and xy-plane at (b) 0.006, (c) 0.06, (d) 0.14, (e) 0.56, and (f) 0.98 H.

561 **Fig. 13.** Time-averaged flow field around the Buddha statue at $\alpha = 90°$ on (a) xz-plane at y/B=0 and xy-plane at

562 (b) 0.006, (c) 0.10, (d) 0.33, (e) 0.52, and (f) 0.75 H.

563 **Fig. 14.** Mean wind force coefficients.

564 **Fig. 15.** (a) Vortex shedding frequency in the wake region (b) Strouhal number

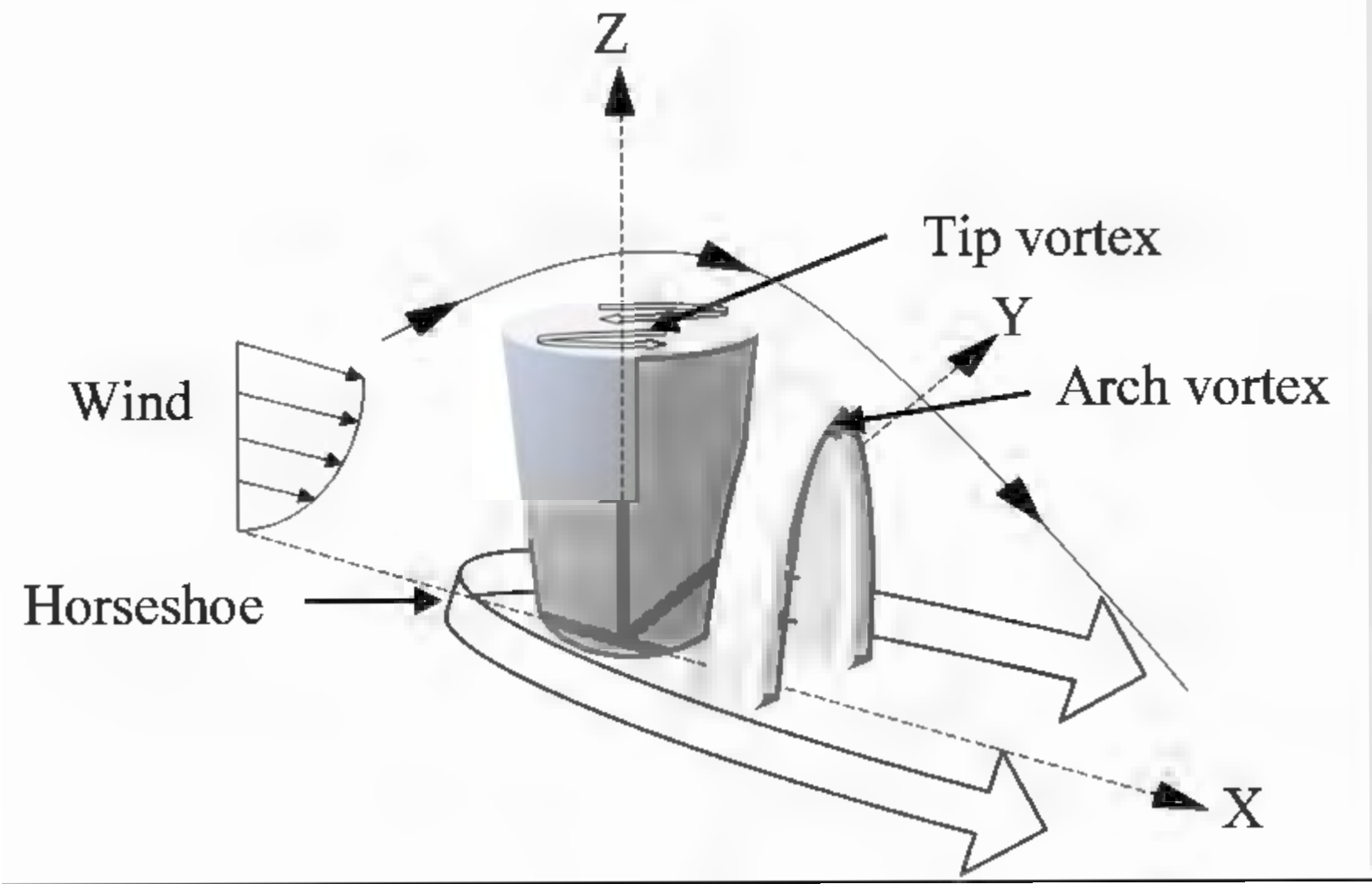
Z
Tip vortex
Y
Wind
Arch vortex
Horseshoe
X

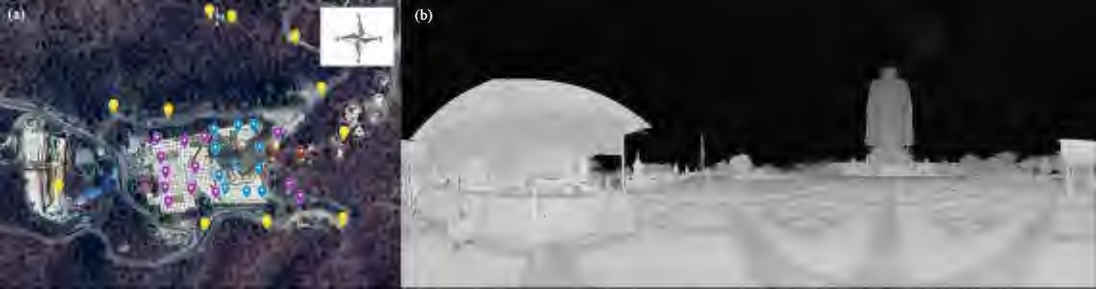
(a)
(b)

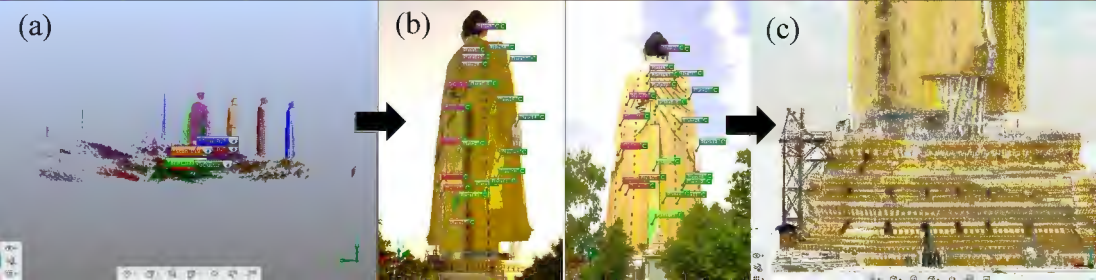
(a)
(b)
(c)

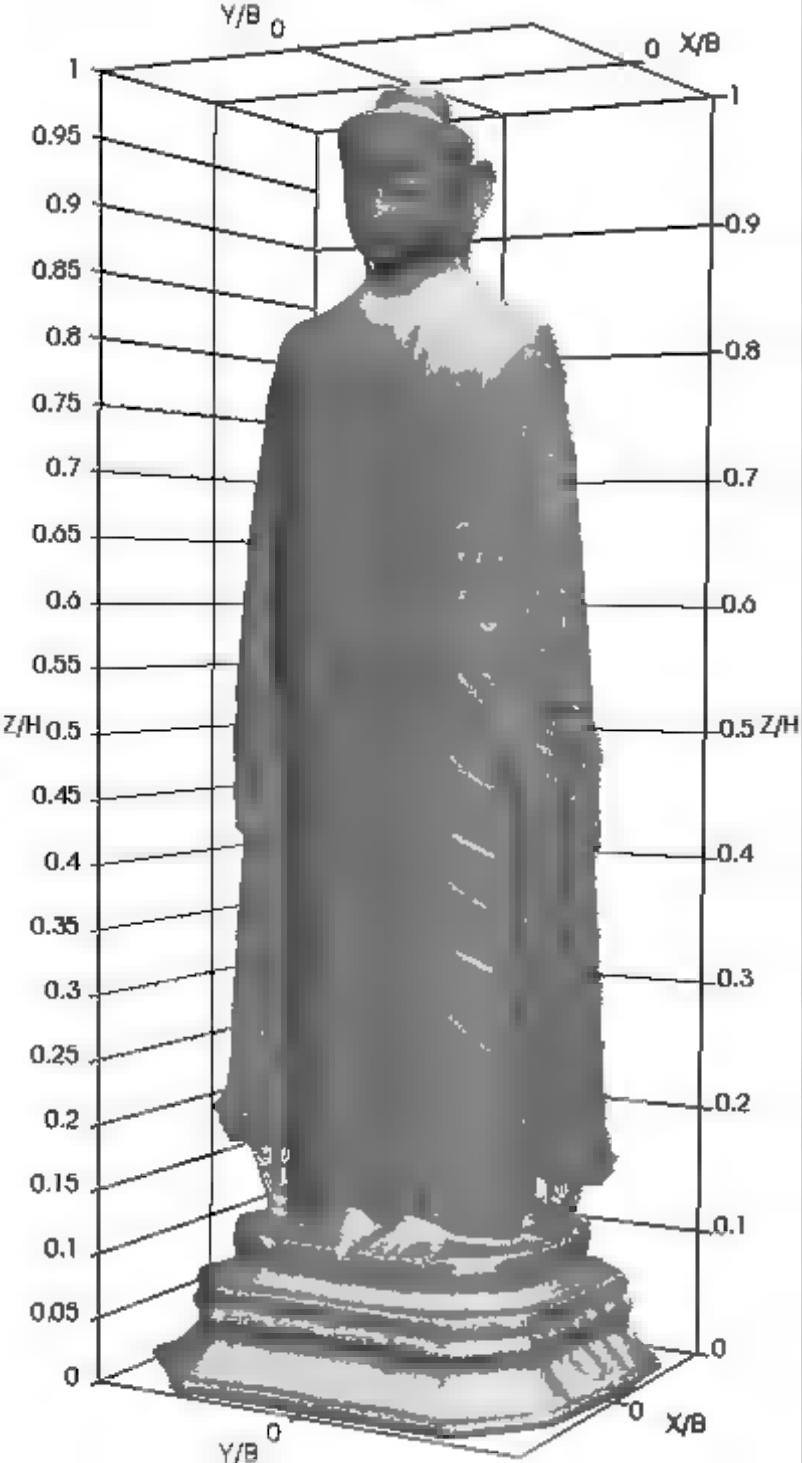
Y/B
0
0
X/B
1
0.95
0.9
0.85
0.8
0.75
0.7
0.65
0.6
0.55
Z/H
0.5
0.45
0.4
0.35
0.3
0.25
0.2
0.15
0.1
0.05
0
1
0.9
0.8
0.7
0.6
0.5
Z/H
0.4
0.3
0.2
0.1
0
0
X/B
Y/B
0

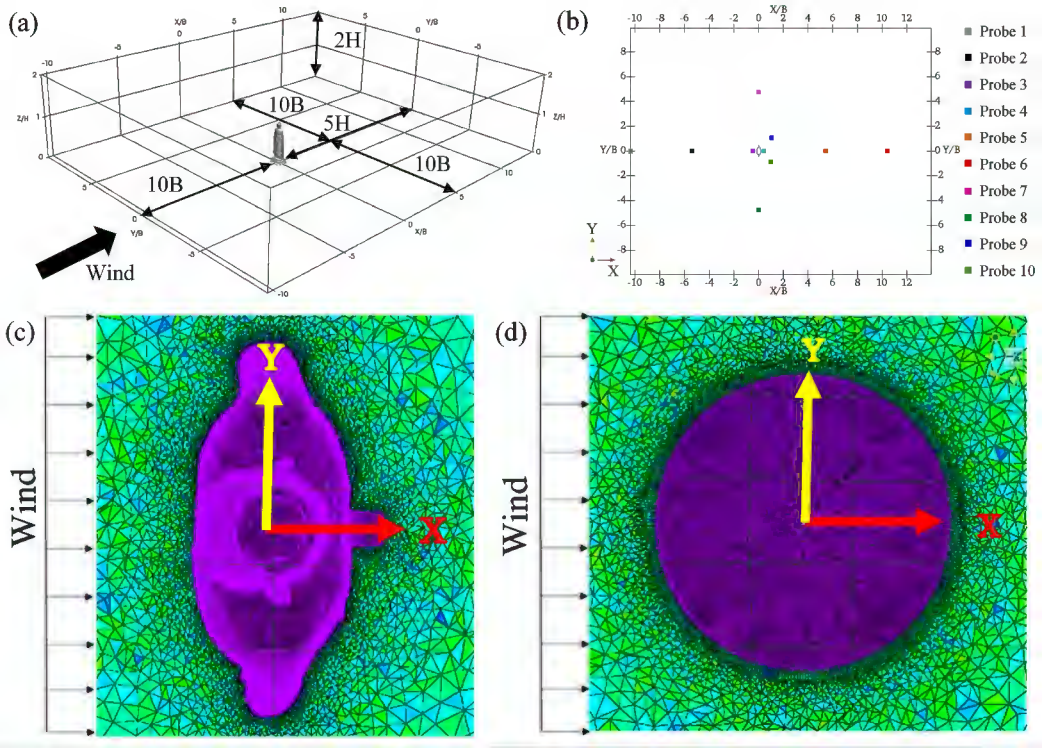
(a)
2H
10B
5H
10B
10B
Wind
X/B
Y/B
Z/H
(b)
Probe 1
Probe 2
Probe 3
Probe 4
Probe 5
Probe 6
Probe 7
Probe 8
Probe 9
Probe 10
X/B
Y/B
Y
X
(c)
Wind
Y
X
(d)
Wind
Y
X

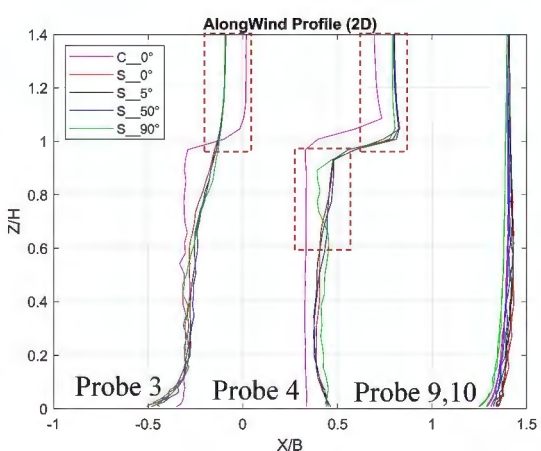
AlongWind Profile (2D)
C__0°
S__0°
S__5°
S__50°
S__90°
Z/H
X/B
Probe 3
Probe 4
Probe 9,10

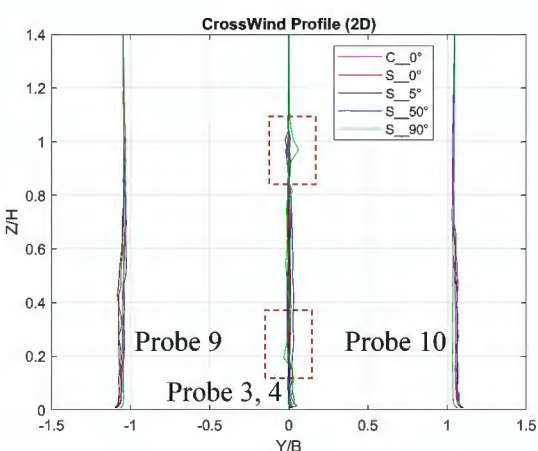
CrossWind Profile (2D)
C__0°
S__0°
S__5°
S__50°
S__90°
Z/H
Y/B
Probe 9
Probe 10
Probe 3, 4

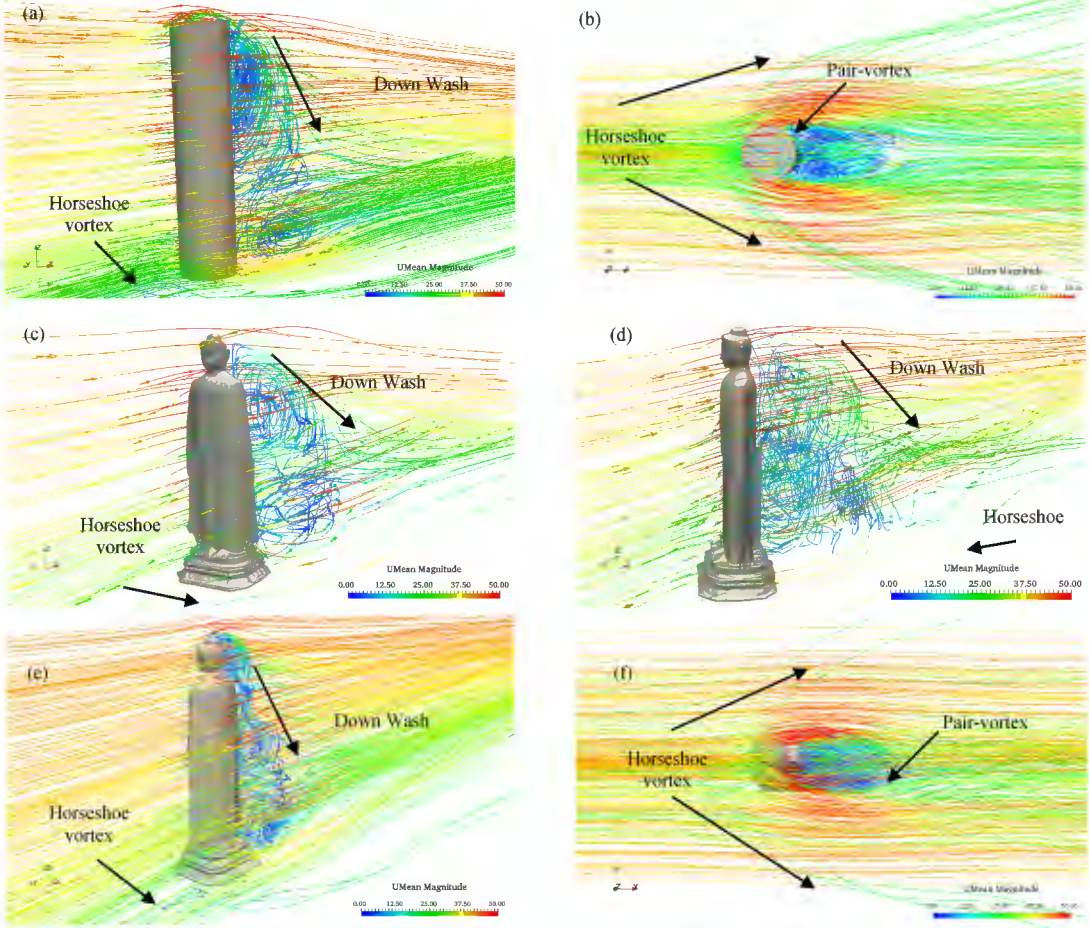
(a)
Down Wash
Horseshoe vortex
UMean Magnitude
0.00 12.50 25.00 37.50 50.00
(b)
Pair-vortex
Horseshoe vortex
(c)
Down Wash
Horseshoe vortex
UMean Magnitude
0.00 12.50 25.00 37.50 50.00
(d)
Down Wash
Horseshoe
UMean Magnitude
0.00 12.50 25.00 37.50 50.00
(e)
Down Wash
Horseshoe vortex
UMean Magnitude
0.00 12.50 25.00 37.50 50.00
(f)
Pair-vortex
Horseshoe vortex

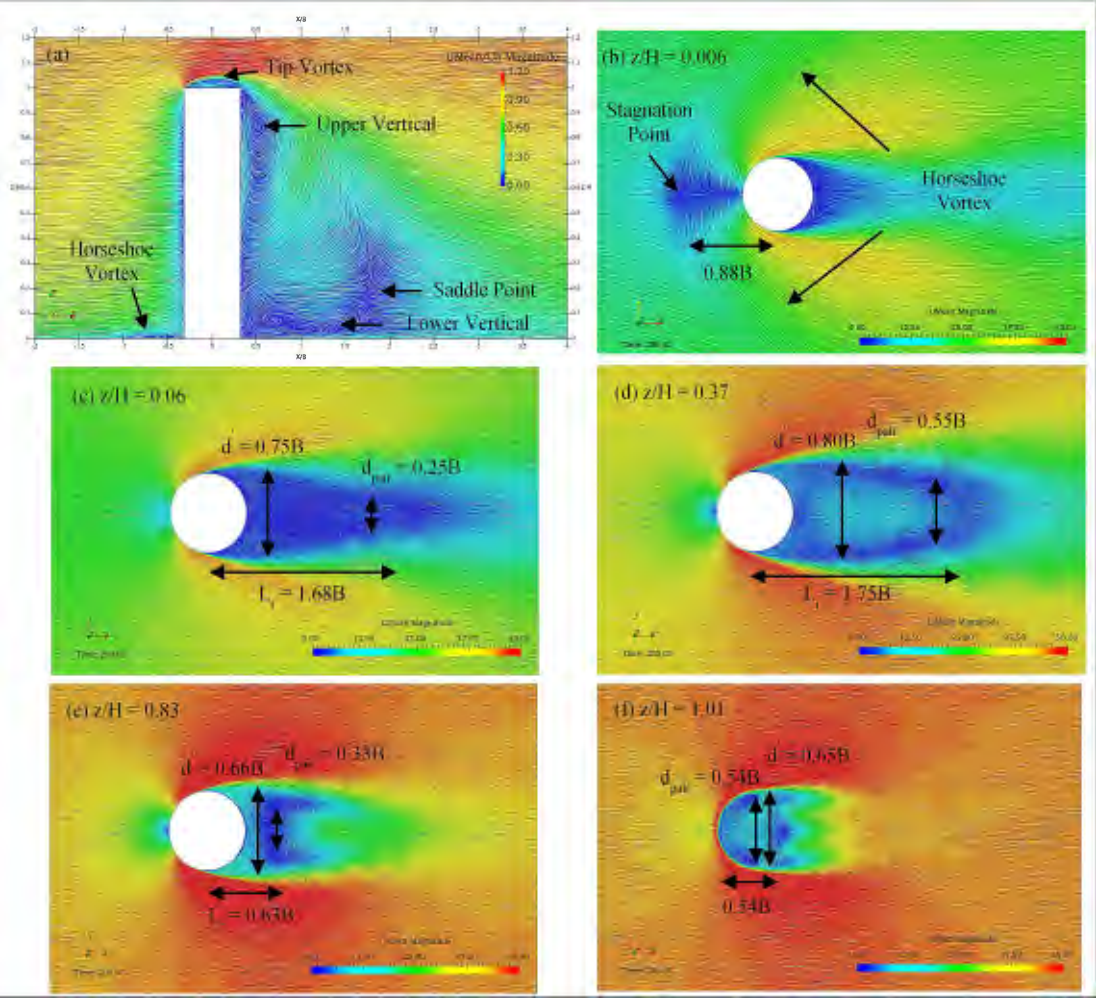
(a)
Tip Vortex
Upper Vertical
Horseshoe Vortex
Saddle Point
Lower Vertical
(b) z/H = 0.006
Stagnation Point
Horseshoe Vortex
0.88B
(c) z/H = 0.06
d = 0.75B
d_pair = 0.25B
L_r = 1.68B
(d) z/H = 0.37
d = 0.80B
d_pair = 0.55B
L_r = 1.75B
(e) z/H = 0.83
d = 0.66B
d_pair = 0.33B
L_r = 0.63B
(f) z/H = 1.01
d = 0.65B
d_pair = 0.54B
0.54B

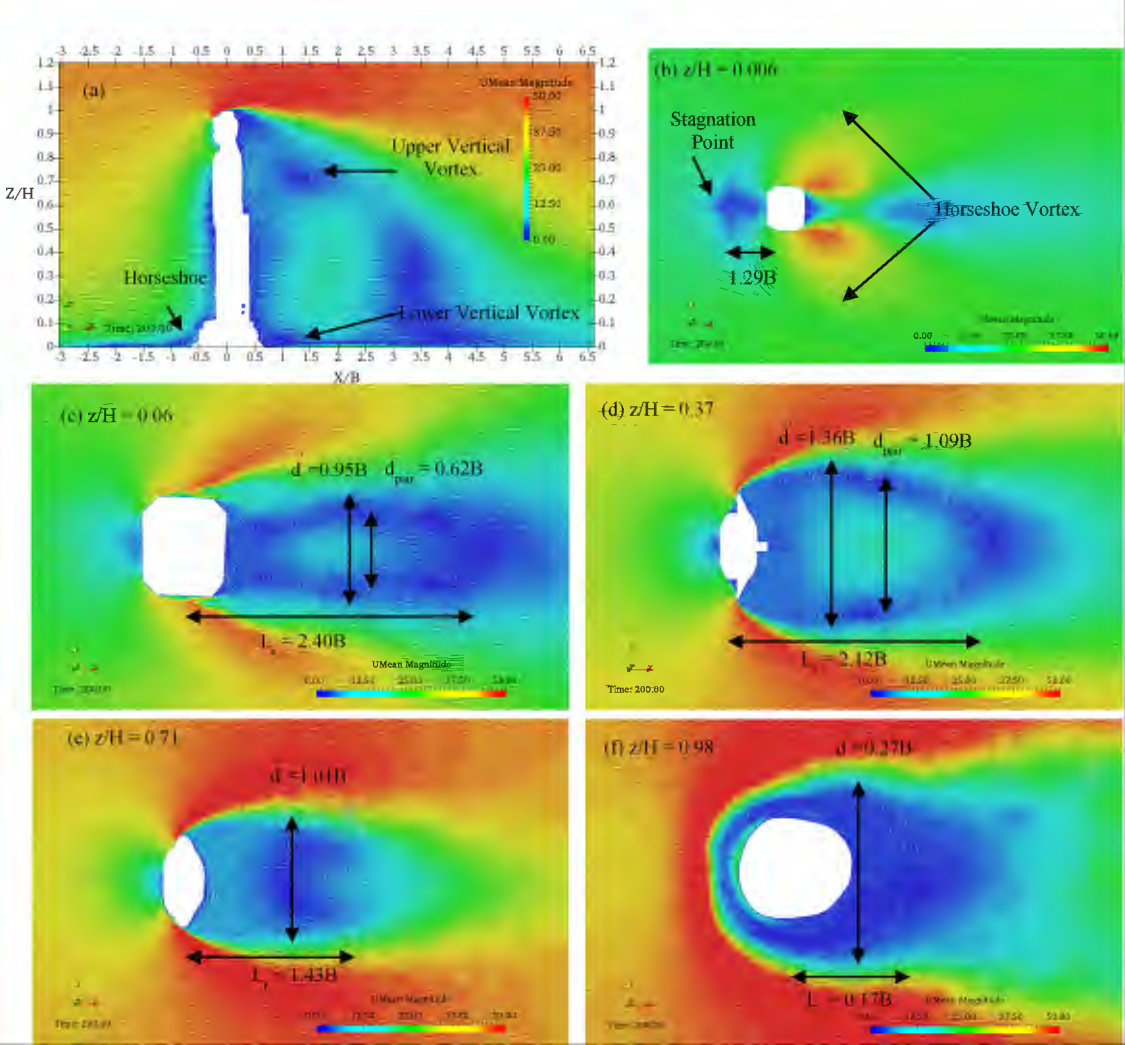
(a)
Upper Vertical Vortex
Horseshoe
Lower Vertical Vortex
Z/H
X/B
(b) z/H = 0.006
Stagnation Point
Horseshoe Vortex
1.29B
(c) z/H = 0.06
d = 0.95B
d_pair = 0.62B
L_s = 2.40B
(d) z/H = 0.37
d = 1.36B
d_pair = 1.09B
L_s = 2.12B
(e) z/H = 0.71
d = 1.01B
L_s = 1.43B
(f) z/H = 0.98
d = 0.27B
L_s = 0.17B

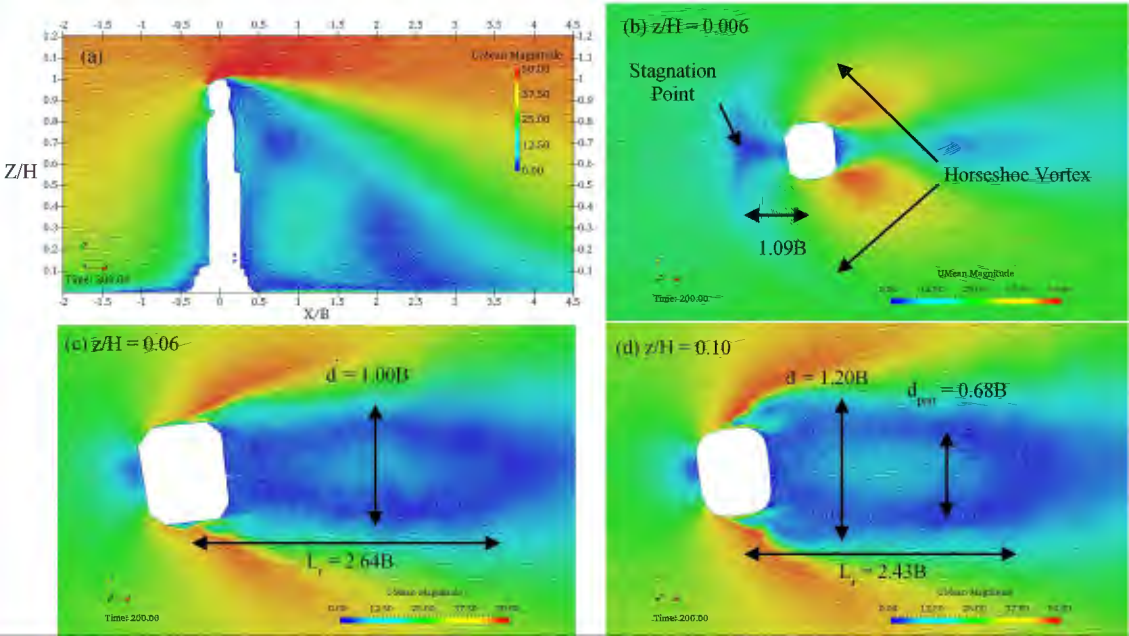
(a)
UMean Magnitude
50.00
37.50
25.00
12.50
0.00
Time: 200.00
Z/H
X/B
(b) z/H = 0.006
Stagnation Point
Horseshoe Vortex
1.09B
UMean Magnitude
Time: 200.00
(c) z/H = 0.06
d = 1.00B
L_r = 2.64B
Time: 200.00
(d) z/H = 0.10
d = 1.20B
d_jet = 0.68B
L_r = 2.43B
Time: 200.00

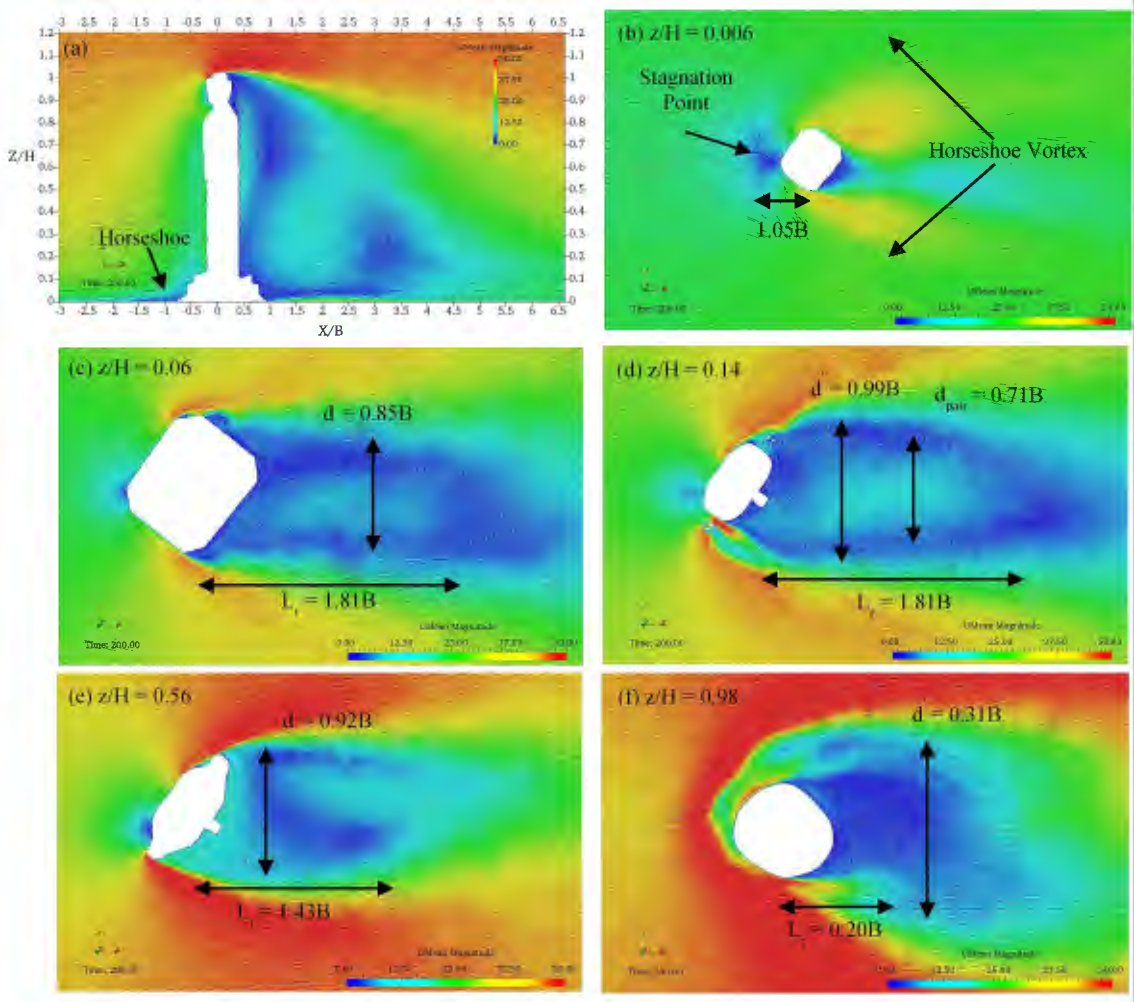
(a)
Horseshoe
Z/H
X/B
(b) z/H = 0.006
Stagnation Point
Horseshoe Vortex
1.05B
(c) z/H = 0.06
d = 0.85B
L_r = 1.81B
(d) z/H = 0.14
d = 0.99B
d_min = 0.71B
L_r = 1.81B
(e) z/H = 0.56
d = 0.92B
L_r = 1.43B
(f) z/H = 0.98
d = 0.31B
L_r = 0.20B

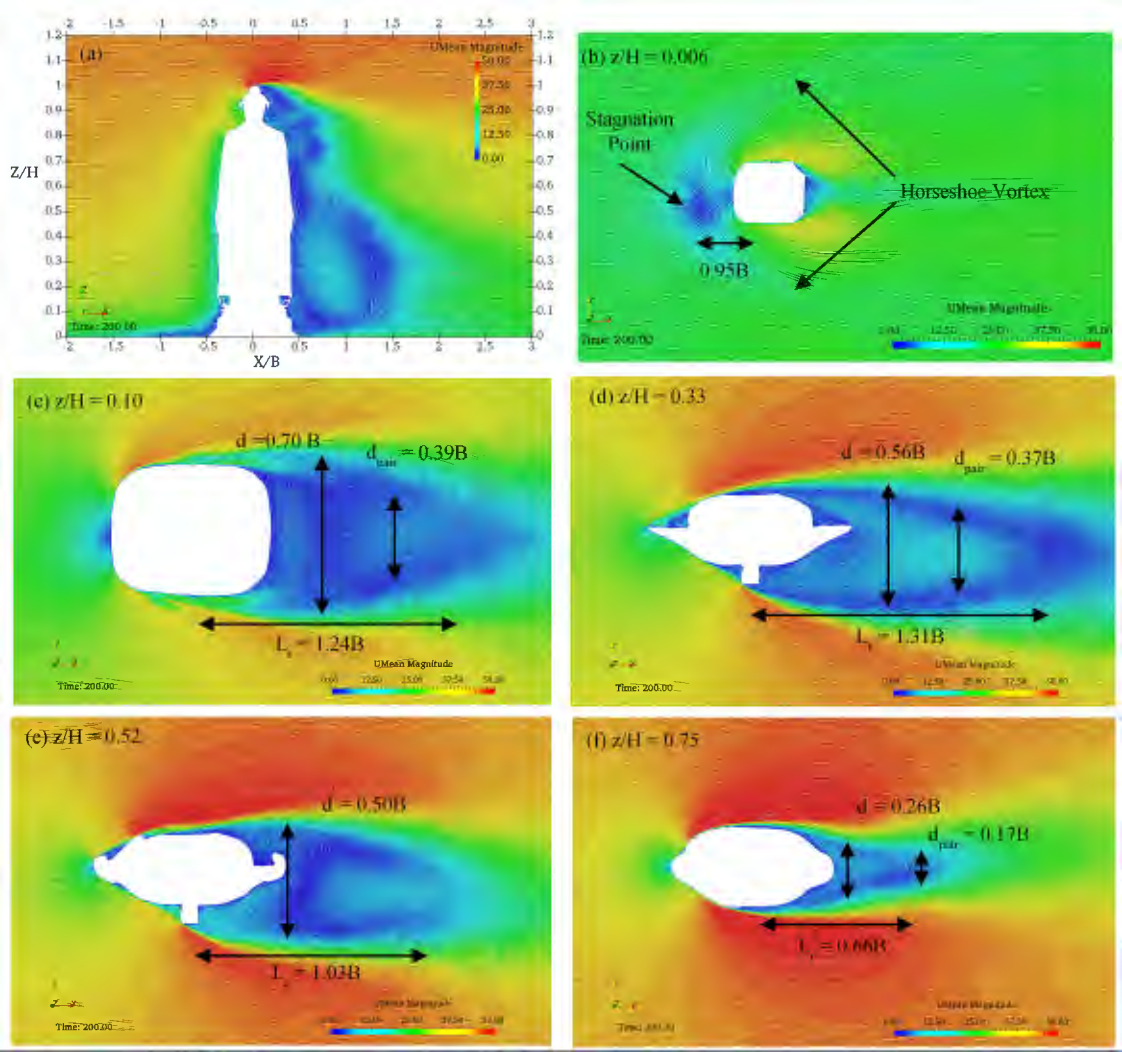
(a)
Z/H
X/B
(b) z/H = 0.006
Stagnation Point
Horseshoe Vortex
0.95B
(c) z/H = 0.10
d = 0.70 B
d_{gap} = 0.39B
L_s = 1.24B
(d) z/H = 0.33
d = 0.56B
d_{gap} = 0.37B
L_s = 1.31B
(e) z/H = 0.52
d = 0.50B
L_s = 1.03B
(f) z/H = 0.75
d = 0.26B
d_{gap} = 0.17B
L_s = 0.66B

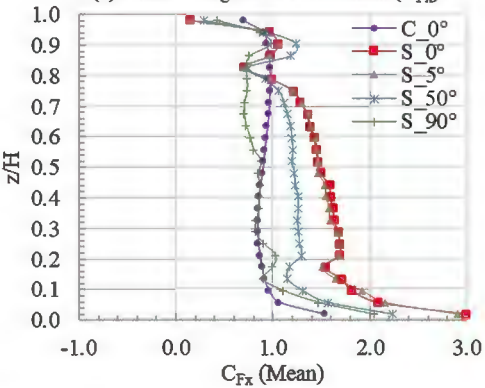
(a) Mean along-wind coefficient (C_{Fx})
z/H
1.0
0.9
0.8
0.7
0.6
0.5
0.4
0.3
0.2
0.1
0.0
-1.0
0.0
1.0
2.0
3.0
C_{Fx} (Mean)
C_0°
S_0°
S_5°
S_50°
S_90°

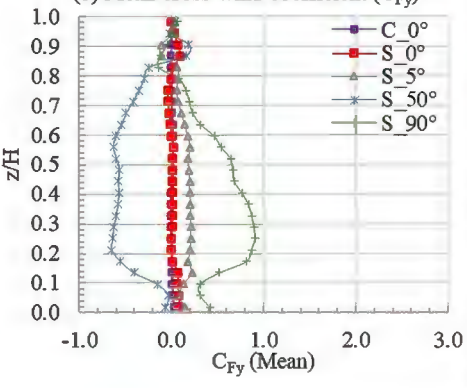
(b) Mean cross-wind coefficient (C_{Fy})
z/H
1.0
0.9
0.8
0.7
0.6
0.5
0.4
0.3
0.2
0.1
0.0
-1.0
0.0
1.0
2.0
3.0
C_{Fy} (Mean)
C_0°
S_0°
S_5°
S_50°
S_90°

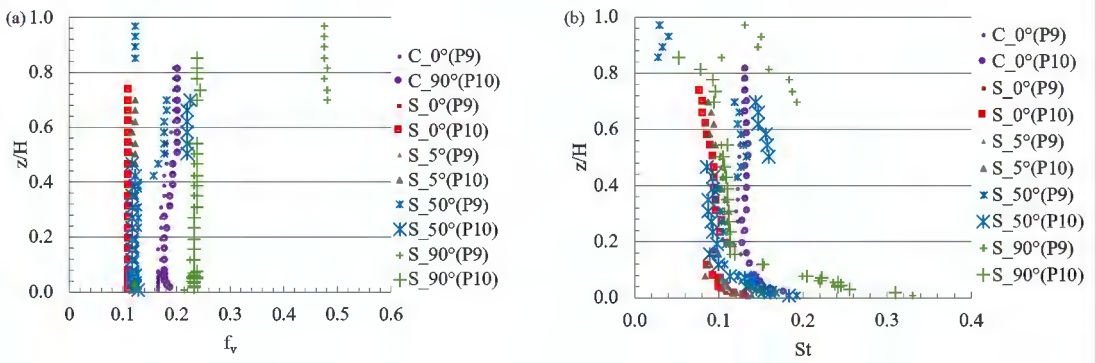
(a)
z/H
f_v
C_0°(P9)
C_90°(P10)
S_0°(P9)
S_0°(P10)
S_5°(P9)
S_5°(P10)
S_50°(P9)
S_50°(P10)
S_90°(P9)
S_90°(P10)
(b)
z/H
St
C_0°(P9)
C_0°(P10)
S_0°(P9)
S_0°(P10)
S_5°(P9)
S_5°(P10)
S_50°(P9)
S_50°(P10)
S_90°(P9)
S_90°(P10)